

Measurement of the fractal order of wall void fraction during nucleate boiling

V. Sathyamurthi ^a, D. Banerjee ^{a,*}, H. Sakamoto ^b, J. Kim ^c

^a Department of Mechanical Engineering, Texas A&M University, College Station, TX 77843, United States

^b NEC Corporation, Sagami-hara, Kanagawa 229–1198, Japan

^c Department of Mechanical Engineering, University of Maryland, College Park, MD 20742, United States

Received 29 August 2006; accepted 22 March 2007

Available online 17 September 2007

Abstract

The fractal nature of hydrodynamic features during nucleate boiling is illustrated in this study. Earlier reports in the literature explored the fractal nature of the thermal features in pool boiling. In these studies typically the time-delay technique was used to obtain chaos quantifiers in boiling from wall temperature fluctuation measurements. In this study experiments were performed at different wall superheats to obtain the images of voids (bubbles) on micro-heaters during nucleate boiling. This study quantifies boiling chaos based on the geometrical features of the voids (e.g., area and perimeter). The fractal order of the geometrical features was obtained by digital image processing. The fractal order (correlation dimension) was computed using the box-counting technique. The experimental apparatus consisted of an array of individually controlled micro-heaters which were used in conjunction with a total internal reflection technique to visualize the wetted area during boiling of FC-72. Images of the voids (bubbles) were captured with a high speed camera. The resulting images were analyzed using the image processing toolbox in MATLAB[®]. Temporal fluctuations observed in the values of the fractal order (for different images in a sequence) were found to remain within distinct bounds with only marginal overlap between the values computed from experimental data obtained at different wall superheats. The fractal order of the voids (based on area, D_{c2}) was found to increase with the wall superheat. This implies that the complexity of the boiling system (represented by the fractal order of the system) increases with wall superheat in nucleate boiling. The fractal order based on perimeter (edge lengths, D_{c1}) of the voids was found to reach a maxima with wall superheat. Furthermore, the plot of D_{c2} versus D_{c1} was found to mimic the conventional boiling curve (wall heat flux versus wall superheat). This shows that D_{c2} and D_{c1} are intrinsically related to wall superheat and heat flux, respectively. Further, it implies that the liquid–vapor contact line plays a major role in modifying pool boiling heat flux compared to the size of the voids (bubbles).

© 2007 Elsevier Inc. All rights reserved.

Keywords: Correlation dimension; Box counting; Critical heat flux; Image processing; Chaos; Fractal; Total internal reflection

1. Introduction

Vast literature exists on utilizing mechanistic models for boiling. Historical development of the mechanistic models can be traced to the classical boiling experiments of Zuber (1959), and Berenson (1961). The earlier classical approaches consisted of developing empirical correlations

from experiments (e.g., Dhir, 1998). The plethora of correlations is not universally applicable because of the inherent limitations imposed by spatio-temporal averaging used in these studies. The efforts at understanding, modeling and predicting the physics of boiling has therefore been restricted by the nature of the experimental data reported in the literature.

The use of non-linear dynamical techniques (e.g., chaos quantifiers) for describing pool boiling phenomena has been attempted by several research groups for the past

* Corresponding author.

E-mail address: dbanerjee@tamu.edu (D. Banerjee).

two decades. Past efforts at evaluating chaos quantifiers from experimental data in boiling can be broadly classified into the following approaches:

- (1) Studies on the effects of wall temperature fluctuations (e.g. Shoji et al., 1995): fractal order of the wall temperature fluctuations was found to increase with superheat until critical heat flux (CHF) and was found to decrease in film boiling.
- (2) Studies on nonlinear aspects of bubble generation (e.g. Shoji, 2004): thermal behavior of nucleation site interactions between bubbles by Zhang and Shoji (2003a,b), and oscillation of bubble surface temperature by Kuzma-Kichta et al. (2000) were observed.
- (3) Studies on the effects of surface roughness on bubble generation and critical heat flux (CHF) by Fong et al. (1998, 2001, 2003).
- (4) Studies on periodicity and bifurcations in boiling in a capillary tube heated by a concentric heated wire by Acharya et al. (2003): the frequency of bubbling was observed to increase non-linearly with increasing heat flux, where linear behavior was observed in the initial phases.

The groups at the University of Tokyo and Oxford University have performed many studies on quantifying boiling chaos (Shoji, 2004) using wall temperature data. Both these groups and others (e.g., Acharya et al., 2003; Sadasivan et al., 1994, 1995a,b) focused their efforts on quantifying chaos in nucleate boiling. Shoji et al. (1995) extended their analyses for quantifying boiling chaos (e.g., Lyapunov exponent, fractal order, attractors, etc.) also to film boiling. Shoji et al. (1995) used chaos quantifiers to analyze the *spatially averaged* experimental data for transient temperature to categorize the various regimes of boiling. Trajectories of the temperature data were reconstructed in the phase space using a time-delay method. The attractors in the phase space were found to gather densely into a narrow space in high heat flux nucleate boiling *suggesting spatial variation*. Thus spatial averaging destroyed the purpose of the modeling effort! In the film boiling regime the attractor was found to have a “wool ball” shape with no trajectory inside (in contrast to the attractor for nucleate boiling). The authors were not able to explain the apparent complexity of this data. This can be explained by the existence of cold spots (Banerjee et al., 1996) (limit cycles) which causes spatio-temporal fluctuations in surface temperature on a fractal scale. Such behavior fits a deterministic chaos model. Amazingly, the authors found that the fractal order (“correlation dimension”) increased with heat flux, formed a peak around CHF and decreased in the film boiling regime.

There is a practical utility of these research efforts which have largely remained unexplored in the past studies reported in the literature. For example, chaos quantifiers can be used to predict the efficacy of various active and passive schemes for thermal management under different

operating conditions (e.g., different superheats). The changes in chaos quantifiers can be linked to the temporal and spatial variations of heat transfer as well as average values of boiling heat transfer coefficients under different conditions (e.g., at different wall superheats). Hence the chaos quantifiers can also be used as a predictive tool.

Past research efforts have primarily explored boiling chaos by investigating thermal features using time-delay techniques (Shoji et al., 1995; Shoji, 2004; Zhang and Shoji, 2003a,b; Kuzma-Kichta et al., 2000; Fong et al., 1998, 2001, 2003; Acharya et al., 2003; Sadasivan et al., 1994, 1995a,b). In this study we explore boiling chaos by investigating hydrodynamic features (voids or bubbles) and evaluate chaos quantifiers (e.g., correlation dimension) using box-counting technique. Previous research efforts in quantifying boiling chaos reported in the literature have largely been restricted to either spatially averaged values of wall temperature fluctuations or spatial variations of temporally averaged values of wall temperature distribution. In this study we report the effect of wall superheat on the fractal order (correlation dimension) of the geometric features of wall void fractions, which vary both spatially and temporally. The geometric features (based on area and perimeter) of the wall void fractions is obtained by using image processing techniques. The uniqueness of this approach is the ability to quantify boiling chaos based on temporal and spatial distribution of hydrodynamic instabilities. The hydrodynamic instabilities manifest through the geometric properties of voids (bubbles) located on the heater surface. The geometric features explored in this study are the contact area of the voids on the heater and the perimeter of the liquid–vapor contact line on the heater (edge length of individual voids or bubbles).

2. Theory

The time dependent aspects of trajectories in non-linear dynamical systems is typically quantified by the Lyapunov exponent and the Kolmogorov–Sinai entropy (Sadasivan et al., 1994). The other class of chaos quantifiers is based on the geometric nature of the attractors. The dimensionality of the attractor is linked to the number of active degrees of freedom of the system. It is known that for a dissipative dynamic system, the dimensionality of the attractor is less than that of the full state space. Furthermore, if an attractor has a noninteger dimension, then it has a strange attractor. These geometric objects of non-integral dimensionalities are termed *fractals*. A measure for the fractal dimension is the *box-counting dimension* also known as *capacity dimension*. However, it is not so useful for higher dimensionality state spaces due to computational limitations. The estimation of box counting dimension is sensitive to the range of box lengths used, due to the limited resolution of data. Nevertheless, it yields a useful first approximation to the fractal dimension. While, the limited resolution of the digitized images may result in an underestimation of counts for smaller boxes resulting in a convex

log–log plot, this can be remedied by the image filtering method proposed by Taylor and Taylor (1991). However, in the present case the log–log plot was a straight line in most cases or else had a good regression coefficient value and thus no special filtering was required.

A brief description of the methodology of the box-counting algorithm is provided here. A detailed description of the method and its underlying philosophy can be found in Hilborn (1994) and Peitgen et al. (2004). Boxes of side A are made to cover the space occupied by the geometric object, i.e. the images in this case. In two dimensions these would be squares and in three dimensions these would be cubes.

The number of boxes (N) needed to cover all points of the geometric object is then found. The size of the boxes is reduced and the above procedure is repeated. This process is carried out so that A tends to zero. As A is decreased the number of boxes required to cover all the points of the object would increase.

The number of boxes (N) is related to the box counting dimension D_b as follows:

$$N(A) = \lim_{A \rightarrow 0} kA^{(-D_b)} \tag{1}$$

Taking the logarithm on both sides yields

$$D_b = \lim_{A \rightarrow 0} \left\{ -\frac{\log N(A)}{\log A} + \frac{\log k}{\log A} \right\} \tag{2}$$

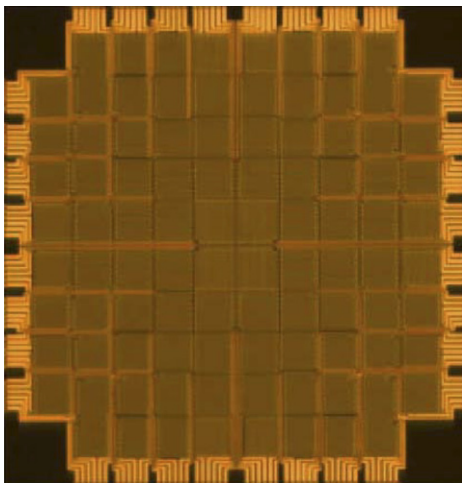
As A tends to zero, the last term in Eq. (2) becomes negligible so the capacity dimension may be obtained as

$$D_b = \lim_{A \rightarrow 0} \left\{ -\frac{\log N(A)}{\log A} \right\} \tag{3}$$

The box counting dimension (D_b) is related to the correlation dimension (D_c) as (Hilborn, 1994):

$$D_c = 1 + D_b \tag{4}$$

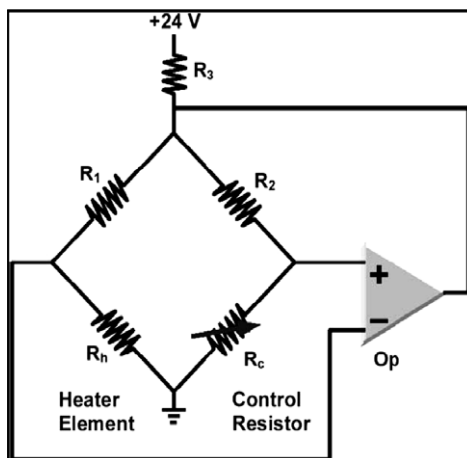
A more detailed description of the box counting algorithm can be found in Hilborn (1994). When the computations



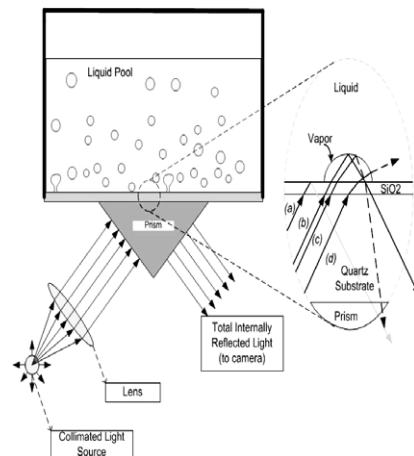
(a) The micro-heater array.

96	95	94	93	92	91	90	89		
65	37	64	63	62	61	60	59	58	88
66	38	17	36	35	34	33	32	57	87
67	39	18	5	16	15	14	31	56	86
68	40	19	6	1	4	13	30	55	85
69	41	20	7	2	3	12	29	54	84
70	42	21	8	9	10	11	28	53	83
71	43	22	23	24	25	26	27	52	82
72	44	45	46	47	48	49	50	51	81
73	74	75	76	77	78	79	80		

(b) Micro-heater array with designated heater numbers and non-working heaters depicted in black.



(c) Schematic of feedback control circuit.



(d) Schematic of the Total internal Reflection Technique for image capture.

Fig. 1. Design of the experimental apparatus.

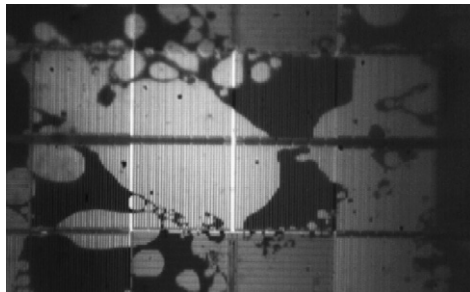
are performed for box counting dimension based on area of the voids it is denoted as D_{c2} . When the computations are performed for box counting dimension based on perimeter (edge length) of the individual voids it is denoted as D_{c1} .

3. Experimental apparatus

Micro heater Array: A micro heater array with total area of 0.49 cm^2 ($7.0 \text{ mm} \times 7.0 \text{ mm}$) was used as the heater surface. The array consisted of 96 heaters each nominally 700 microns in size, similar to that used in a previous study (Horacek et al., 2005). A picture of the array is shown in Fig. 1. Each heater element consisted of a thin (200 nm thick, $7 \mu\text{m}$ wide) serpentine platinum resistance heater. The heater was sputtered onto a tungsten adhesion layer that was deposited on a $500 \mu\text{m}$ thick quartz substrate. The effective temperature coefficient of resistance of the metallic layer was approximately $0.002 \text{ }^\circ\text{C}^{-1}$, and the length, width, and thickness of the serpentine elements were designed to provide a nominal resistance of approximately 180Ω . Thicker gold leads were deposited up to the edge of the array to ensure minimal lead resistance ($<1 \Omega$), and the entire array was covered with a $1 \mu\text{m}$ SiO_2 passivation layer to provide a uniform surface energy.

Individual heater elements were maintained at a constant specified temperature through the use of 96 separate Wheatstone bridge feedback circuits, one of which is illustrated schematically in Fig. 1c. The temperature of the element was selected through the use of a $20 \text{ k}\Omega$ digital potentiometer with 512 discrete steps. When combined with the other resistor elements in the circuit, this provided for an effective temperature regulation ranging from $30 \text{ }^\circ\text{C}$ to $110 \text{ }^\circ\text{C}$ with a resolution of approximately $0.3 \text{ }^\circ\text{C}$. In the current configuration, each heater is capable of dissipating 1.3 W , or a maximum surface heat flux of up to 250 W/cm^2 . The settings for the digital potentiometer were calibrated through the use of an insulated, constant-temperature, calibration oven. A feedback controller was used to maintain a constant interior oven temperature, while the threshold setting of the digital potentiometer that just started regulation of the circuit was determined. The calibration was performed on each of the heater elements in $5 \text{ }^\circ\text{C}$ increments between $60 \text{ }^\circ\text{C}$ to $100 \text{ }^\circ\text{C}$, in addition to one at $30 \text{ }^\circ\text{C}$. During the experiments, two 64-channel 12-bit analog-to-digital conversion boards were used to sample data from each individual heater at 1000 Hz .

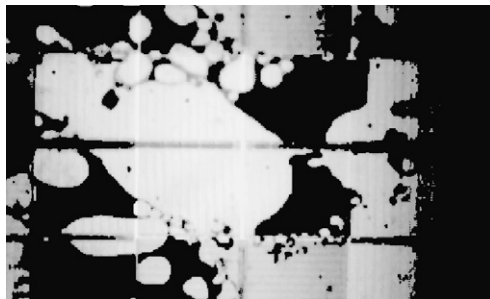
Use of a transparent quartz substrate combined with the 50% coverage area of the serpentine heater element allowed for visualization of the impacting spray by looking through the quartz substrate. A high-speed digital camera (Vision



(a) Initial unprocessed image.



(b) Processed image after contrast adjustments and removal of structural components of the heater by threshold operation.



(c) Processed image after background homogenization.



(d) Cropped binary image. White areas denote voids.

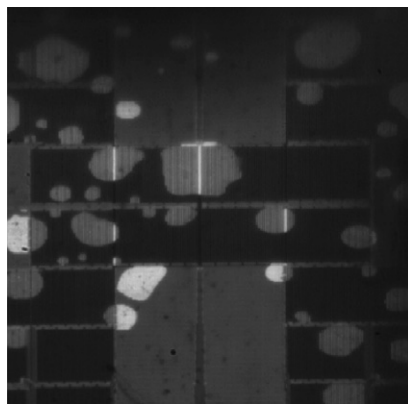
Fig. 2. Image processing operations performed for obtaining a binary image of the voids (bubbles) for calculating the correlation dimension (D_{c2}). (Wall temperature = $90 \text{ }^\circ\text{C}$, Image #1.)

Research Phantom v4.0) capable of acquiring 512×512 pixel images at speeds of up to 1000 fps was used to record the images. The camera was configured to run with a reduced sensor size of 128×512 pixels, operating at 1000 fps, and was synchronized to the data acquisition system of the heater array. A tele-microscope lens (Infinity KC with IF3 objective) provided variable magnification imaging (0.9X–1.3X) with a working distance of 15 cm to 19 cm. The lens and camera were adjusted to provide a clear image of 8 heaters in a 2×4 formation on the array surface (heaters marked numbers 1, 2, 3, 4, 9, 10, 15, 16 in Fig. 1b).

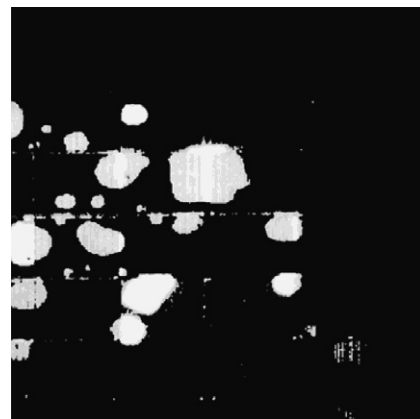
3.1. Total internal reflection technique

The TIR technique has been used in the past to study spray cooling (Horacek et al., 2005, 2003, 2004), droplet impact (Lee et al., 2001) and pool boiling (Lee et al., 2002; Yaddanapudi and Kim, 2001; Demiray and Kim, 2004; Myers et al., 2005; Yin et al., 2004). Areas of liquid–solid contact area were obtained using the total internal reflection (TIR) technique shown schematically on Fig. 1d. A right angle prism (index of refraction, $n = 1.517$) was placed in contact with the underside of

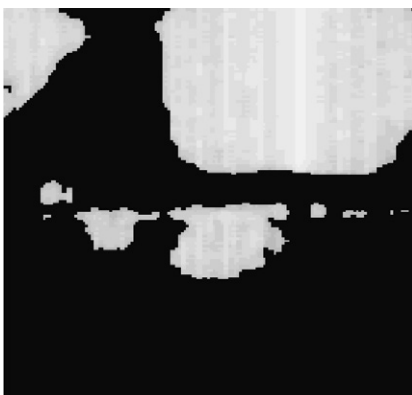
the quartz substrate ($n = 1.544$) containing the heater array. An optical immersion oil ($n = 1.52$) ensured that no air gap existed between the prism and the substrate. Light from a collimated source was then positioned such that total internal reflection of the light occurred at the interface between the SiO_2 passivation layer ($n = 1.46$) and the vapor in the chamber ($n = 1.00$), resulting in a bright area on the image (see ray trace (a) in Fig. 1d). The critical angle for total internal reflection from SiO_2 to a vapor is approximately 43° , which conveniently allowed the use of a 45° prism to direct the light onto the substrate. If liquid was present, then the light traveled past the liquid–quartz interface and was scattered at the liquid–air interface, forming a dark region on the image. A small percentage of light was reflected directly from the SiO_2 /liquid interface, but calculations showed this to be less than 4% of the incident light. Due to the relatively small aperture and long working distance of the lens ($f\# \sim 10$), light that was scattered at the liquid/vapor interface but was not parallel to the lens axis was not imaged. The only exception to this was at locations where the slope of the interface was nearly parallel to the SiO_2 surface. For the small surface features observed under most conditions, these points were typically confined to regions below the



(a) Processed Image after contrast adjustment.



(b) Processed image after contrast adjustments and removal of structural components of the heater by threshold operation.



(c) Processed images after background homogenization and cropping.



(d) Cropped binary Image with detected edges.

Fig. 3. Image processing operations performed for obtaining a binary image of the voids (bubbles) and edge detection of the voids for calculating the correlation dimension (D_{c1}). (Wall temperature = 83°C , Image #1.)

resolution of the camera. An example of the type of image that could be obtained is shown in Fig. 2a, under conditions where the wall temperature was close to CHF. The dark areas indicate liquid on the surface. The heater area covered by liquid and the length of the three-phase contact line could easily be determined with appropriate image processing (discussed below).

4. Results

Two sets of experimental data were analyzed in this study. Sequence of images were obtained from movies recorded at different wall superheat. FC-72 was used as the working fluid in the experiments (saturation temperature = 57 °C).

4.1. Image analysis

The acquired images in a sequence at each wall superheat were analyzed using the image processing toolbox in MATLAB®. Digital images were obtained from individual frames of the recorded movie files during the boiling experiments. The digital images were imported as gray-scale images into MATLAB® (Fig. 2a).

The following sequence of steps was then performed. The contrast of the images was adjusted using the histogram equalization via a built-in function in the image processing software (Fig. 2b). In order to remove bias errors introduced by structural features (heater elements) present in the image, filtering operation was performed based on an intensity threshold. The differences in the intensities of the void fractions and the heater elements allowed the elimination of the heater elements by the filtering operation. This

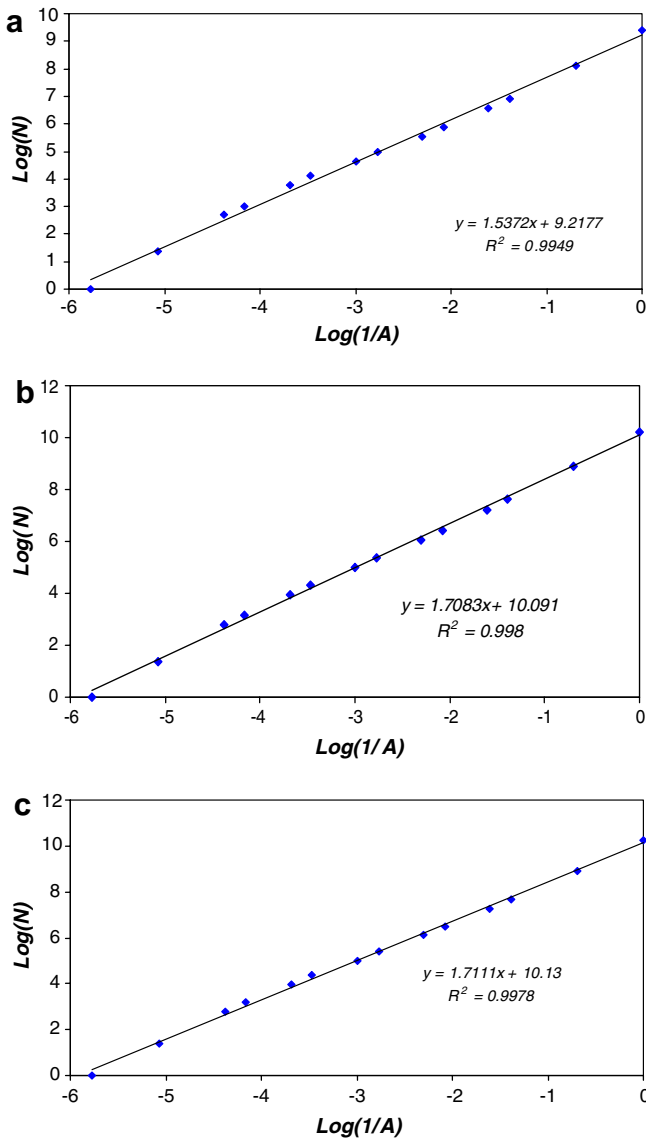


Fig. 4. Representative plots for obtaining the box counting dimension (D_b for D_{c2}) for the first experimental run's first frame: (a) Wall temperature = 80 °C, Image #1; (b) Wall temperature = 83 °C, Image #1 and (c) Wall temperature = 85 °C, Image #1.

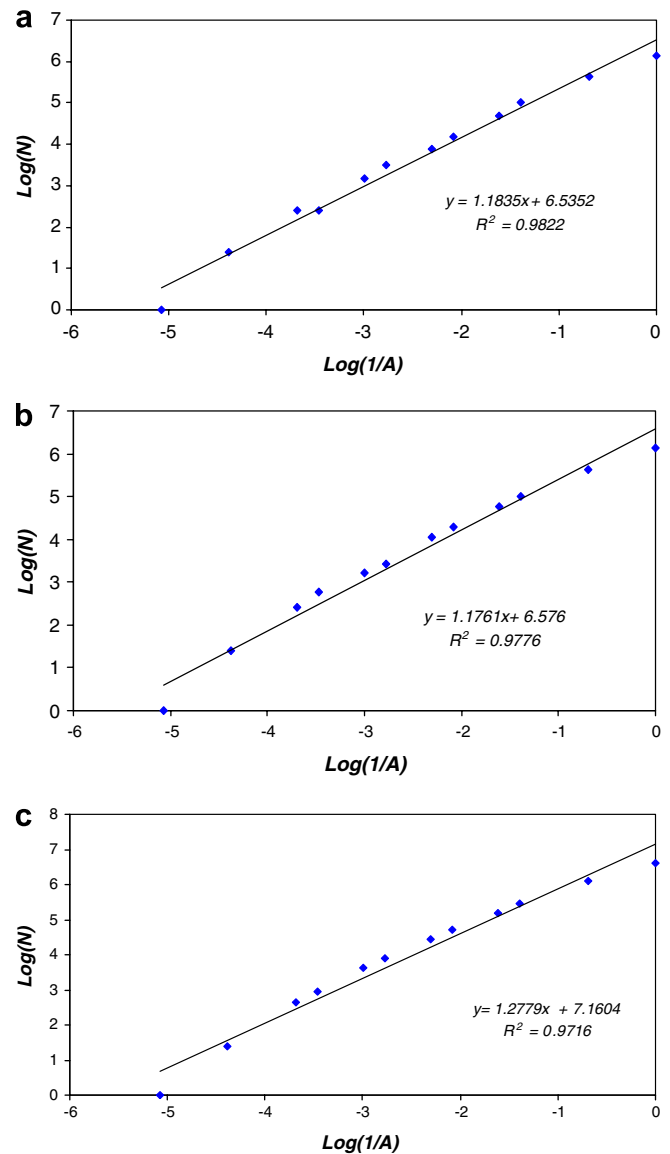


Fig. 5. Plots for obtaining the box counting dimension (D_b for D_{c1}). The slope of the graph corresponds to D_b .

step was necessary to eliminate errors in the calculation of areas of bubbles (surface void fraction based on area) due to partial reflection from the heater elements. The threshold however, varied slightly from one image to the next in a given image sequence that was obtained for a particular experiment. Hence the global optimum value for intensity threshold for all the images in a sequence was obtained by evaluating the intensity threshold for individual images. After determining the optimum threshold value this was applied to all images in a given sequence. In order to eliminate variations in background intensity, a structural element much larger than the bubbles was used to determine the background intensity. The processed image was then subtracted from the intensity image (Fig. 2c). In order to prevent the blurred portions of the image from affecting the results, the processed file obtained above was cropped to a uniform square of 320 pixels \times 320 pixels for the first experimental run and a uniform square region of 256 pixels \times 256 pixels for the second experimental run. Selection of the region to be cropped was based on the quality of the processed image vis-à-vis the original image. For the first and second experimental runs this corresponded to the central regions of the image. The same region was selected in the complete sequence of images for image processing. The images thus obtained were then converted to binary image (Fig. 2d) with the pixels occupying the voids were marked with a value of 1 and the pixels not occupying the void region were marked with a value of 0. This binary image was used for quantitative analysis of wall void fraction (based on area) using the box counting algorithm. It must be remarked here that the sequence of steps in the image processing to obtain binary images for the wall void fractions (such as intensity homogenization and threshold intensity values) was consistent in each sequence of images and varied for the different sequences (e.g., Figs. 3a and b).

The above procedure was also repeated on the sequence of images for edge detection of the voids. The edge detection served to delineate the liquid-vapor contact line on the heater surface. The edge-detection was performed with the built-in Canny algorithm in the MATLAB[®] tool box. The Canny algorithm was consistently found to have a superior performance for edge detection in this study compared to the Sobel algorithm. Using the edge detection algorithm binary images were produced where the pixels identified as the edges of the voids were marked with a value of 1 and the pixels in the rest of the binary image were marked with a value of 0. The representative results of the steps involved in image processing are shown in Figs. 3a through d.

4.2. Box counting dimension

The box counting algorithm was used for analyzing the geometric features associated with the voids (bubbles) on the heater surface. The geometric features examined in the present study were: area of the voids and perimeter of the liquid-vapor contact line on the heater surface (edge length).

The algorithm for box counting decremented box sizes in specific ratios based on the number of pixels on each side of the cropped binary image. For our case these ratios were factors of 320 for the first experimental run and factors of 256 for the second experimental run. For a given box size, the number of boxes which enclosed a part of the bubble (Fig. 2d) was counted in calculating D_{c2} . For a given box size, the number of boxes which enclosed a part of the liquid-vapor contact line (Fig. 3d) was counted in calculating D_{c1} .

The boxes which contained a bubble or a part of a bubble were flagged to a value of one. The number of such boxes (N) corresponding to a given box size (with side of length A) was then obtained by summing all the boxes with a flag of one. Thus for each image a table was generated with box sizes as the first column and the number of boxes as the second column. For each image the fractal order for wall void fraction (based on area, D_{c2}) was obtained by plotting a graph. The resulting graph of $\ln(N)$ vs. $\ln(1/A)$ is plotted in Fig. 4 and the slope is calculated. Representative graphs are shown in Figs. 4a–c. The slope of the graphs yields D_b . The correlation dimension (D_{c2}) is obtained by incrementing D_b by one (Eq. (4)).

Similarly, the boxes which contained a part of the liquid-vapor contact line (Fig. 3d) were flagged to a value of 1. The number of such boxes (N) corresponding to a given box size (with side of length A) was then obtained by summing all the boxes with a flag of 1. Thus for each image a table was generated with box sizes as the first column and the number of boxes as the second column. For

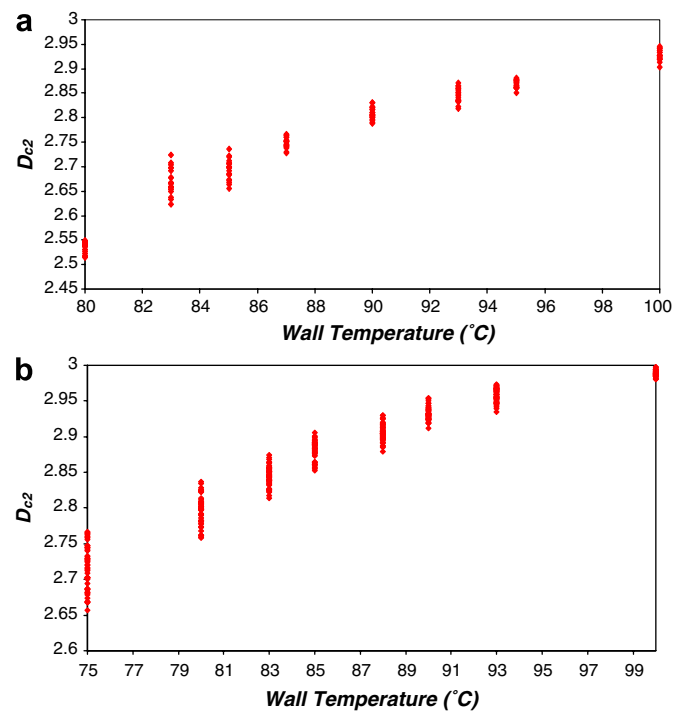


Fig. 6. Variation of fractal order (D_{c2}) with wall temperature in nucleate boiling for two experiments.

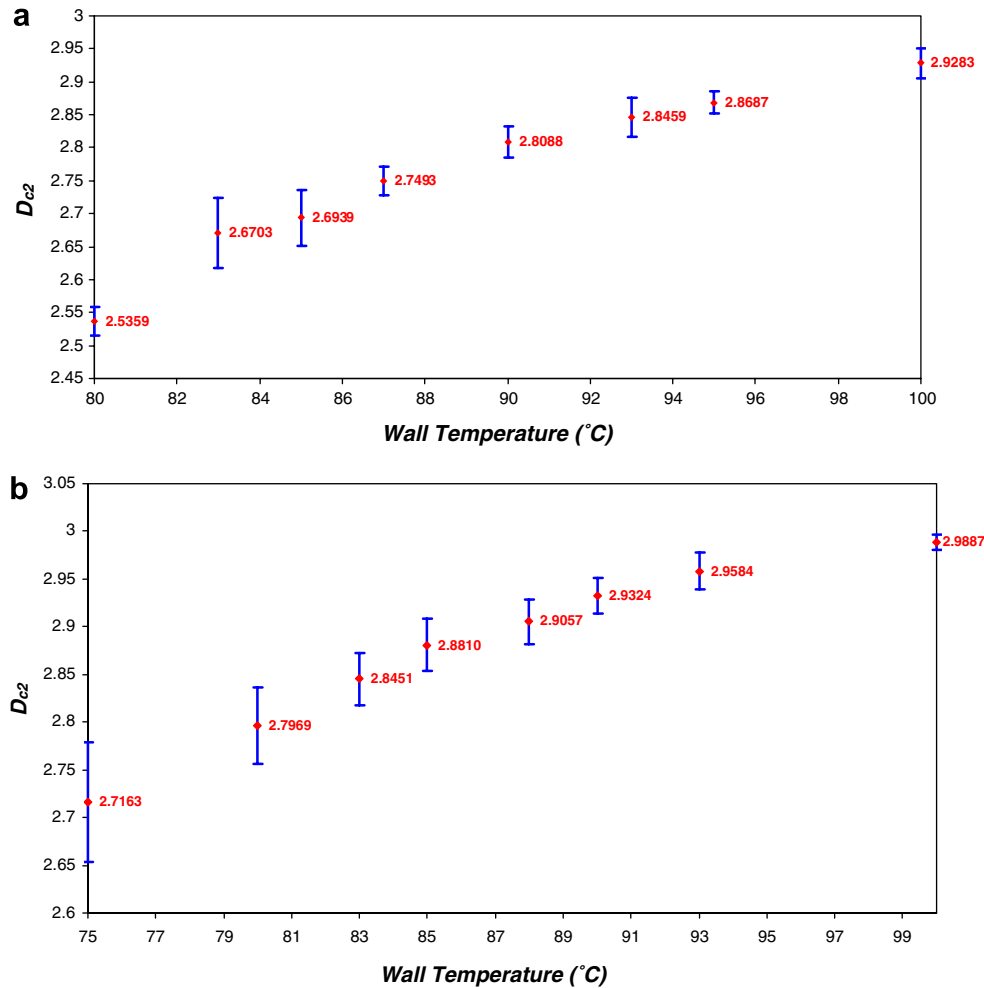


Fig. 7. Variation of the mean values of the fractal orders (D_{c2}) obtained at each superheat with wall temperature in nucleate boiling for two experiments.

each image the fractal order for wall void fraction (based on edge length, D_{c1}) was obtained by plotting a graph. The resulting graph of $\ln(N)$ vs. $\ln(1/A)$ is plotted in Fig. 5 and the slope is calculated. Representative graphs are shown in Figs. 5a–c. The slope of the graphs yields D_b . The correlation dimension (D_{c1}) is obtained by incrementing D_b by one (Eq. (4)).

Fig. 6 shows the values of D_{c2} plotted as a function of wall temperature for different superheats. The results show that the fractal order (D_{c2}) increases monotonously with wall temperature (and therefore the wall superheat). In Fig. 6 the plotted values of D_{c2} obtained at a particular superheat show a certain amount of variability as they vary temporally from image to image in each sequence of images recorded in the experiments. It is observed from Fig. 6 that the temporal fluctuations observed in the values of the fractal order (D_{c2}) for different images in a sequence remain within distinct bounds with only marginal overlap between the values obtained at different wall superheats. Also, the fractal order of the voids was observed to vary marginally with changes in the orientation of the images but the qualitative trends remained the same.

The mean values of D_{c2} were plotted in Fig. 7 along with the error/uncertainty estimates marked by the error bar. The mean value is listed at each wall temperature in the figure. The uncertainty estimate was taken to be equal $\pm 2\sigma$ for 95% confidence interval (where σ is the standard deviation in the data in Fig. 6 for a given wall temperature). The mean values of D_{c2} and the ranges of variation (reflected by the standard deviation values) are distinctly different for the different superheats. The results show that the relative change in fractal order (D_{c2}) decreases closer to the critical heat flux (CHF) point (i.e., at higher superheats) and reaches an asymptotic value of 3. This can be expected since closer to the CHF point the wall void fraction (based on area) would approach an asymptotic value which can be estimated from linear stability analysis for Helmholtz instability to be approximately $(\pi/16)$ for an infinite heater (Lienhard and Dhir, 1973). At this condition (CHF) the system possibly acquires a deterministic character (hydrodynamically speaking) and therefore approaches an integer value.

Fig. 8 shows the values of D_{c1} plotted as a function of wall temperature for different superheats. The data for

D_{c1} shows a larger degree of variability (than D_{c2} as plotted in Figs. 6 and 7). In Fig. 8 the plotted values of D_{c1} obtained at a particular superheat show a certain amount of variability as they vary temporally from image to image in each sequence of images recorded in the experiments. It is observed from Fig. 8 that the temporal fluctuations observed in the values of the fractal order (D_{c1}) for different images in a sequence have considerable overlap between the values obtained at different wall superheats. The variability is found to be larger for wall temperatures exceeding 88 °C. This large variability can be explained by the smaller number of pixels that are involved in calculation of D_{c1} (since it involves pixels along the edges only) compared to the larger number of pixels involved in calculation of D_{c2} (since it involves pixels covered by the whole area of the voids). Hence D_{c1} is expected to have a larger error and therefore a larger variability in the computed values.

The results plotted in Fig. 8a for D_{c1} as a function of wall temperature show that the fractal order increases with wall temperature (and therefore the superheat) until a wall temperature of ~90 °C. Beyond this wall temperature the data shows a marginal decrease in the fractal order (which

is subsequently verified in Fig. 9a). The results plotted in Fig. 8b also show a similar trend. However, there is a marked decrease in values of D_{c1} for temperatures exceeding 90 °C in the second experiment.

The mean values of D_{c1} were plotted in Fig. 9 along with the error/uncertainty estimates marked by the error bar. The mean value is listed at each wall temperature in the figure. The uncertainty estimate was taken to be equal $\pm 2\sigma$ for 95% confidence interval (where σ is the standard deviation in the data in Fig. 8 for a given wall temperature). The mean values of D_{c1} are found to reach a maximum value close to 90 °C followed by a marginal decrease in the first experiment (Fig. 8a) and a marked decrease in the second experiment (Fig. 8b). This shows that D_{c1} is not a strong function of wall superheat but some other experimental parameter (e.g., heat flux).

The relationship between D_{c1} and D_{c2} at different superheats was explored in Fig. 10. It is observed that in the first experiment (Fig. 10a) D_{c1} increases with D_{c2} and reaches a maxima at $D_{c1} = 2.3$ and $D_{c2} = 2.85$. This is followed by a marginal decrease in the value of D_{c1} with increase in D_{c2} . In the second experiment (Fig. 10b) the maxima occurs at

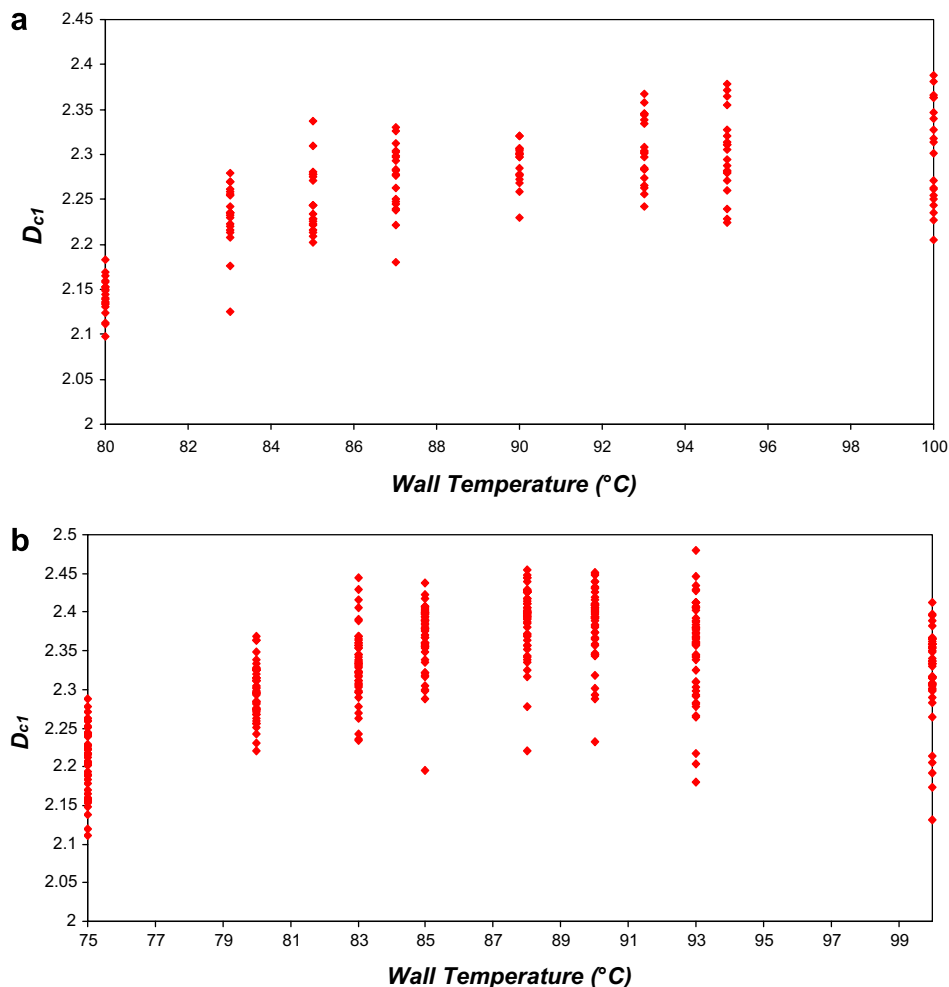


Fig. 8. Variation of fractal order (D_{c1}) with wall temperature in nucleate boiling for two experiments.

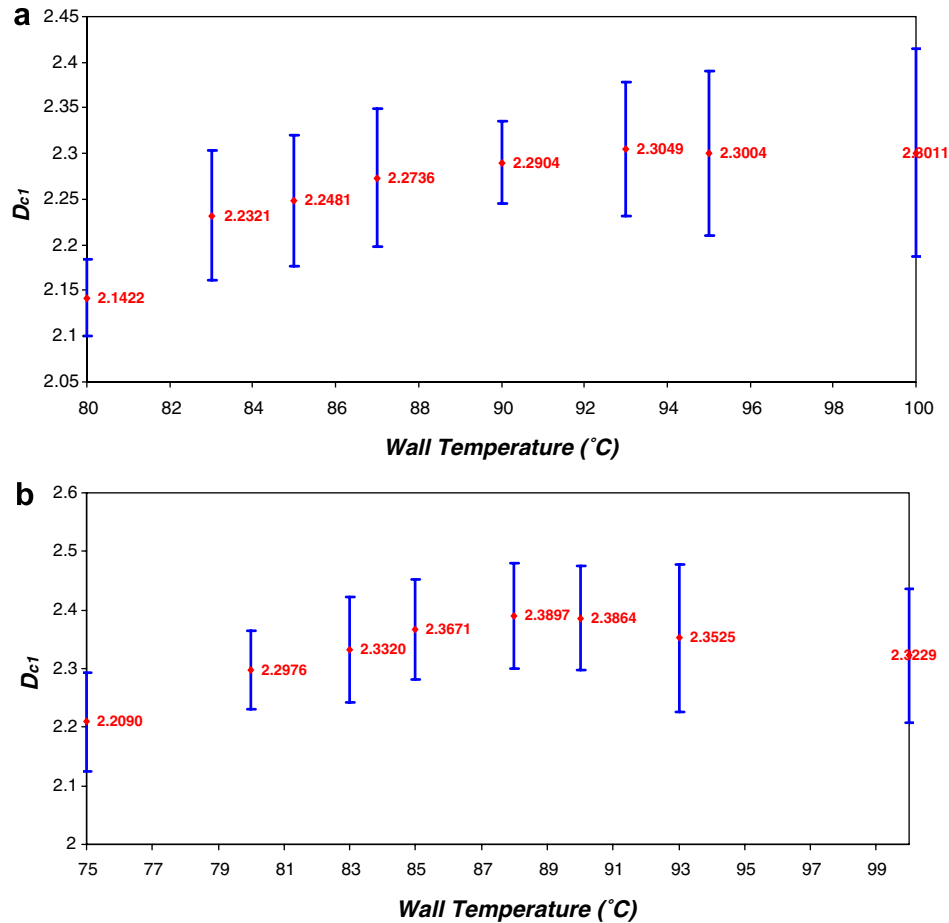


Fig. 9. Variation of mean values of fractal order (D_{c1}) with wall temperature in nucleate boiling for two experiments.

$D_{c1} = 2.39$ and $D_{c2} = 2.9$ which is followed by marked decrease in D_{c1} with increase in D_{c2} . The magnitude of the final decrease of D_{c1} in the second experiment is observed to be $\sim 50\%$ of the magnitude of the increase to the peak value.

Fig. 10a is found to mimic the boiling curve for the first experiment which is plotted in Fig. 11. In Fig. 11 the area averaged heat flux values are plotted as a function of heater temperature (which is same as wall superheat + 57 °C). The heat flux values reach a maxima at the critical heat flux (CHF) corresponding to a wall temperature of 100 °C. Similar trend is observed for the corresponding values of D_{c1} and D_{c2} plotted in Fig. 10b. This shows that D_{c1} is strongly affected by the area averaged heat flux during pool boiling. Whereas, the results plotted in Figs. 6 and 7 show that D_{c2} is strongly related to the wall temperature (or wall superheat).

5. Conclusions

1. The fractal orders for geometrical properties of voids (area and edge length) in nucleate boiling were computed as well as their variation with wall superheat and averaged heat flux was analyzed.
2. Boiling chaos was quantified based on hydrodynamic instabilities (wall void fraction) and using the box-counting technique. This is a distinctly different approach for exploring boiling chaos compared to reported methods in the literature (which have conventionally explored boiling chaos by monitoring the thermal instabilities).
3. Temporal fluctuations for D_{c2} remained within distinct bounds and were found to marginally overlap for the different wall superheats.
4. The temporal fluctuation for D_{c1} was found to be more widely distributed (compared to D_{c2}) and were found to overlap for a wide range of wall superheats.
5. The correlation dimension in nucleate boiling was found to asymptote to a value close to 3.0 as superheat was increased toward CHF. This shows that the degrees of freedom of a boiling system increases with superheat and approaches an integer value. This shows that the hydrodynamic instabilities acquire a deterministic character at CHF.
6. The plot of D_{c1} versus D_{c2} was found to mimic the boiling curve for pool boiling.
7. The fractal order based on area of the voids (D_{c2}) was found to increase with the wall superheat.

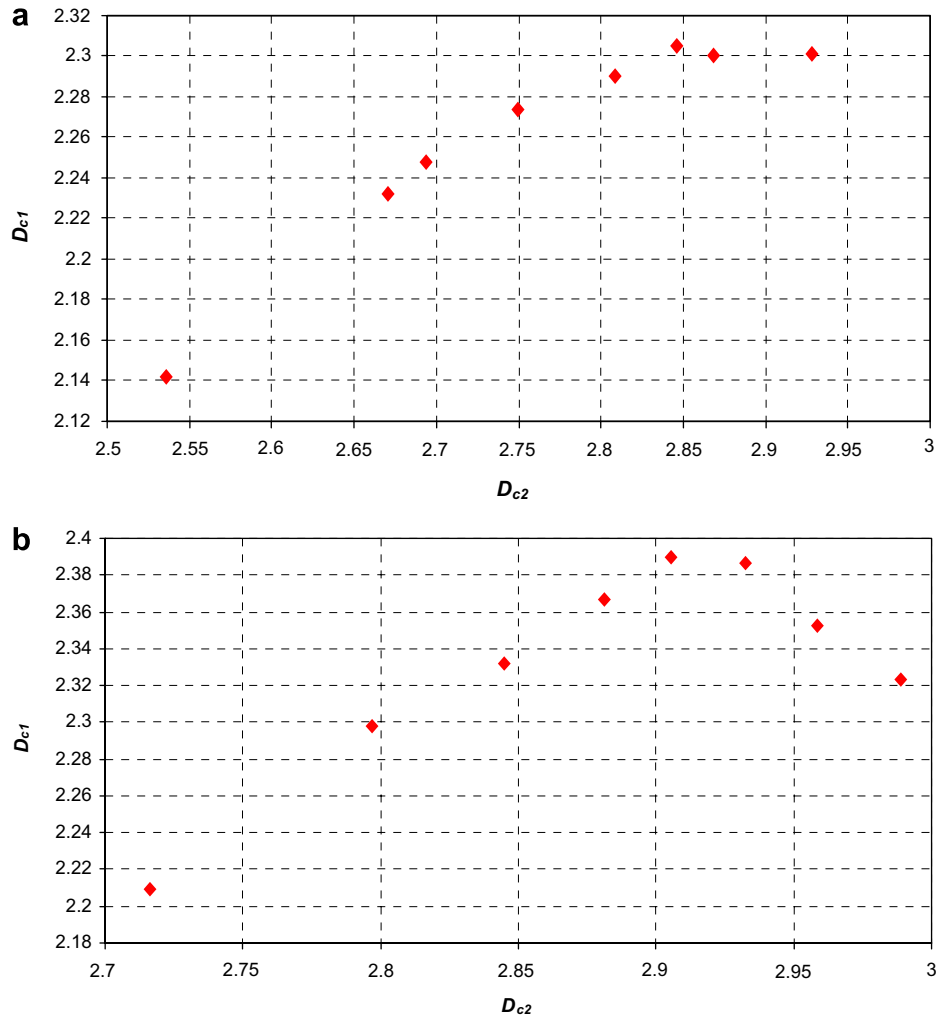


Fig. 10. Plot of mean values of D_{c1} versus mean values of D_{c2} that were obtained at the corresponding wall superheat from the two experiments. The plot is similar to the boiling curve for the experiments (see Fig. 11).

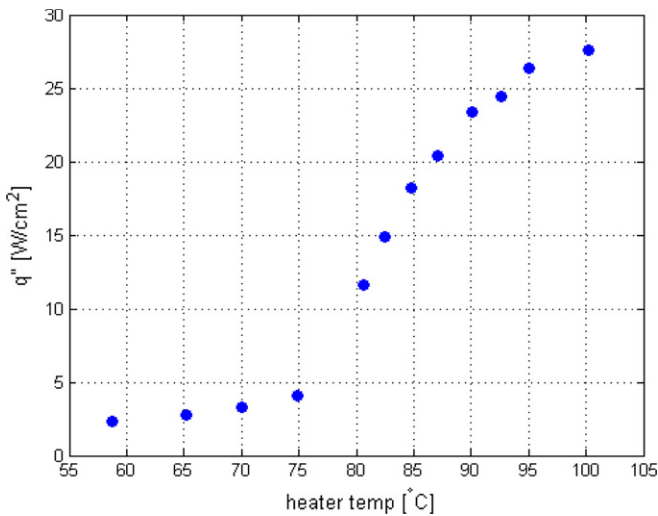


Fig. 11. Boiling curve for the first experiment showing the area averaged wall heat flux plotted against the heater temperature (or wall superheat + 57 °C). Saturation temperature of FC-72 used as a working fluid in the experiments is 57 °C.

8. The fractal order based on edge length of the voids (D_{c1}) was found to be related to the area averaged wall heat flux.

6. Scope for future work

Additional experiments can be performed in conjunction with improvement in the image acquisition and analysis techniques. Such improvements can provide insights into the detailed nature of the dependence of D_{c1} on area averaged wall heat flux (global heat flux) as well as local values of wall heat flux fluctuations. Additional experiments can be performed to explore the directional dependence of D_{c1} on heat flux. For example, D_{c1} values obtained by computing edge lengths from advancing segment of the liquid–vapor contact line may be more sensitive to the local heat flux (and global heat flux) as compared to the receding contact line. Additional computational algorithms can be developed to compute D_{c1} values based on the location of the edge lengths on the

advancing or receding contact lines. Furthermore, the standard deviation in D_{c1} (and possibly D_{c2}) values may be reduced if the structural features of the heater can be removed from the images more efficiently.

References

- Acharya, N., Sen, M., Ramos, E., 2003. Periodicity and bifurcations in capillary tube boiling with a concentric heater wire. *International Journal of Heat and Mass Transfer* 46, 1425–1442.
- Banerjee, D., Son, G., Dhir, V.K., 1996. Conjugate thermal and hydrodynamic analyses of saturated film boiling from a horizontal surface. In: *Proceedings of the 1996 International Mechanical Engineering Congress and Exposition*, Atlanta, GA.
- Berenson, P.J., 1961. Film boiling heat transfer from horizontal surface. *J. Heat Transfer* 83, 351–362.
- Demiray, F., Kim, J., 2004. Microscale heat transfer measurements during pool boiling of FC-72: Effect of subcooling. *International Journal of Heat and Mass Transfer* 47, 3257–3268 (744 KB).
- Dhir, V.K., 1998. Boiling heat transfer. *Annual Review of Fluid Mechanics* 30, 365–401.
- Fong, R.W.L., Coleman, C.E., Nitheanandan, T., Kroeger, V.K., Moyer, R.G., Sanderson, D.B., Root, J.H., Rogge, R.B., et al., 1998. External glass peening of zircalloy calandria tubes to increase the critical heat flux. In: *Proceedings of the Eleventh Pacific Basin Nuclear Conference*, Banff, Alberta, Canada, May 3–7, (also in AECL-11898).
- Fong, R.W.L. et al., 2001. Correlation between the critical heat flux and the fractal surface roughness of Zirconium alloy tubes. *Journal of Enhanced Heat Transfer* 8, 137–146.
- Fong, R.W.L., Nitheanandan, T., Bullock, C.D., Slater, L.F., McRae, G.A., et al. 2003. Effects of oxidation and fractal surface roughness on the wettability and critical heat flux of glass-peened Zirconium alloy tubes. In: *Proceedings of the Fifth International Conference on Boiling Heat Transfer*, Montego Bay, Jamaica, May 4–8, (also in AECL-12169).
- Hilborn, 1994. *Chaos and Non-linear Dynamics, An Introduction for Scientists and Engineers*. Oxford University Press, New York.
- Horacek, B., Kim, J., Kiger, K., 2003. Effects of noncondensable gas and subcooling on the spray cooling of an isothermal surface. In: *Proceedings of the ASME IMECE*, paper no. IMECE2003-41680.
- Horacek, B., Kim, J., Kiger, K., 2004. Spray cooling using multiple nozzles: visualization and wall heat transfer measurements. *IEEE Transactions on Device and Materials Reliability* 4 (4), 614–625.
- Horacek, B., Kiger, K., Kim, J., 2005. Single nozzle spray cooling heat transfer mechanisms. *International Journal of Heat and Mass Transfer* 48 (8), 1425–1438.
- Kuzma-Kichta, Y., Ustinov, A.K., Ustinov, A.A., Kholpanov, L., 2000. Investigation by laser and acoustic method of interface oscillations during boiling. In: *Proceedings of the Engineering Foundation Conference on Boiling Phenomena and Emerging Applications*, Alaska, USA, , pp. 100–115.
- Lee, J., Kim, J., Kiger, K.T., 2001. Time and space resolved heat transfer characteristics of single droplet cooling using microscale heater arrays. *International Journal of Heat and Fluid Flow* 22, 188–200.
- Lee, J., Kiger, K.T., Kim, J., 2002. Enhancement of droplet heat transfer using dissolved gases. In: *SAE 2002 Transactions Journal of Aerospace*, pp. 736–746.
- Lienhard, J.H., Dhir, V.K., 1973. Hydrodynamic prediction of peak pool boiling heat fluxes from finite bodies. *Journal of Heat Transfer* 95, 152–158.
- Myers, J.G., Yerramilli, V.K., Hussey, S.W., Yee, G.F., Kim, J., 2005. Time and space resolved wall temperature and heat flux measurements during nucleate boiling with constant heat flux boundary conditions. *International Journal of Heat and Mass Transfer* 48 (12), 2429–2442 (952 KB).
- Peitgen, Heinz-Otto, Jürgens, Harmut, Saupe, Dietmar, 2004. *Chaos and Fractals, New Frontiers of Science*, second ed. Springer-Verlag.
- Sadasivan, P., Unal, C., Nelson, R., 1994. Non-linear aspects of high heat flux nucleate boiling heat transfer, Part 2: Results. In: *ASME Winter Annual Meeting*, Chicago, HTD 298, pp. 91–102.
- Sadasivan, P., Unal, C., Nelson, R.A., 1995a. Nonlinear aspects of high heat flux nucleate boiling heat transfer. *Journal of Heat Transfer* 117, 981–989.
- Sadasivan, P., Unal, C., Nelson, R.A., 1995b. The need for new experiments. *Journal of Heat Transfer* 117, 558–567.
- Shoji, Masahiro, 2004. Studies of boiling chaos: a review. *International Journal of Heat and Mass Transfer* 47, 1105–1128.
- M. Shoji, T. Kohno, J. Negishi, S. Toyoshima, A. Maeda. 1995. Chaos in boiling on a small-size heater. In: *Proceedings of the Fourth ASME-JSME Thermal Engineering Joint conference*, Maui, vol. 2, pp. 225–232.
- Taylor, C.C., Taylor, S.J., 1991. Estimating the dimension of a fractal. *Journal of the Royal Statistical Society Series, B-Methodological* 53, 353–364.
- Yaddanapudi, N., Kim, J., 2001. Single bubble heat transfer in saturated pool boiling of FC-72. *Multiphase Science and Technology* 12 (3–4), 47–63.
- Yin, Z., Prosperetti, A., Kim, J., 2004. Bubble growth on an impulsively powered microheater. *International Journal of Heat and Mass Transfer* 47 (5), 1053–1067.
- Zhang, L., Shoji, M., 2003a. Nucleation site interaction in pool boiling on the artificial surface. *International Journal of Heat and Mass Transfer* 46, 513–522.
- Zhang, L., Shoji, M., 2003. Nucleation site interaction in pool boiling – Experimental study by employing artificial boiling surface. In: *Proceedings of the Fifth ASME-JSME Thermal Engineering Joint Conference*, Hawaii, March 16–20.
- Zuber, N., 1959. *Hydrodynamic Aspects of Boiling Heat Transfer*. Ph.D. Thesis, University of California, Los Angeles.